Reflectance Spectroscopy of Chromium-bearing Spinel with Application to Recent Orbital Data from the Moon

K.B. Williams, C.R.M. Jackson, L.C. Cheek, K.L. Donaldson Hanna, S.W. Parman, C.M. Pieters, M.D. Dyar, T.C. Prissel

Abstract

Visible to near-infrared (V-NIR) remote sensing observations have identified spinel in a variety of locations and lithologies on the Moon. Experimental studies have quantified the FeO content of these spinels (Jackson et al., 2014), however the chromite component is not well constrained. Here we present compositional and spectral analyses of spinel synthesized with varying chromium contents at lunar-like oxygen fugacity (fO_2). Reflectance spectra of the chromium-bearing synthetic spinels (Cr# 1-29) have a narrow (~130 nm wide) absorption feature centered at ~550 nm. The 550 nm feature, attributed to octahedral Cr^{3+}, is present over a wide range in iron content (Fe# 8-30) and its strength positively correlates with spinel chromium content [$\ln(\text{reflectance}_{min}) = - 0.0295\ Cr\# - 0.3708$]. Our results provide laboratory characterization for the visible to near-infrared (V-NIR) and mid-infrared (mid-IR) spectral properties of spinel synthesized at lunar-like fO_2. The experimentally determined calibration constrains the Cr# of spinels in the lunar Pink Spinel Anorthosites to low values, potentially Cr# < 1. Furthermore, the results suggest the absence of a 550 nm feature in remote spectra of the Dark Mantle Deposits at Sinus Aestuum precludes the presence of a significant chromite component. Combined, the

observation of low chromium spinels across the lunar surface argues for large contributions of anorthositic materials in both plutonic and volcanic rocks on the Moon.

Introduction

Recent analyses of Chandrayaan-1 Moon Mineralogy Mapper (M^3) and SELENE Kaguya Spectral Profiler (SP) orbital data have identified spinel-bearing lithologies across the lunar surface (e.g., Sunshine et al., 2010; Pieters et al., 2011; Dhingra et al., 2011a, 2011b; Yamamoto et al., 2013; Pieters et al., 2014; Sunshine et al., 2014). Detections of these previously unresolved surface components provide new insight into the petrogenesis and evolution of the lunar crust.

Most remotely detected spinels are Mg- and Al-rich ("Mg-spinel") and are thought to be mixed with high proportions of plagioclase based on their prominent 2000 nm absorption feature and relatively high albedos. This new rock type has been termed "pink spinel anorthosite" (PSA, e.g. Taylor and Pieters, 2013; Pieters et al., 2014) and has been found globally (Pieters et al. 2010, 2011, 2013, 2014; Sunshine et al., 2010; Dhingra et al. 2011a, 2011b; Lal et al., 2011, 2012; Dhingra and Pieters, 2011; Kaur et al., 2012, 2013a, 2013b; Bhattacharya et al., 2012, 2013; Donaldson Hanna, 2013; Yamamoto et al., 2013; Sun et al. 2013; Kaur and Chauhan, 2014). Additionally, unique low-albedo regions identified within the Sinus Aestuum pyroclastic deposits are suggested to be rich in Fe- or Cr-rich spinel due to their spectral signature near 1000 nm (Sunshine et al., 2010, 2014; Yamamoto et al., 2013). The specific nature of each spinel-bearing lithology remains uncertain and several petrogenetic models have been proposed, including melt-rock reaction and impact melting (Gross and Treiman, 2011;

Yamamoto et al., 2013; Prissel et al., 2014, Gross et al., 2014). Constraining the composition of the remotely sensed lunar spinels is fundamental in identifying plausible formation mechanisms.

Previous laboratory investigations have typically focused on characterizing terrestrial spinels (e.g., Cloutis et al., 2004). Spectral comparison with terrestrial spinels suggests PSA lithologies contain Mg-spinel similar to those found in pink spinel troctolites. However, terrestrial spinels form under more oxidizing conditions than lunar spinels, leading to relatively high ferric iron contents. Ferric iron in terrestrial spinels is expressed across the spectral range of M^3 and SP, obscuring the connection to lunar spinels (Figure 1). In this context, we conducted the current study to explore the spectral effects of chromium on well-characterized lunar analog spinel.

In contrast to the Mg-, Al-rich composition inferred for the remotely sensed spinels, Apollo samples and lunar meteorites mostly contain Cr- and Fe-rich spinels (Haggerty, 1971, 1972, 1973, 1977). A small number of samples (e.g., spinel troctolites, Mg-suite samples) contain spinels similar to those remotely detected. The apparent overrepresentation of Mg-spinels in remote sensing observations may be due to the ease of detecting Mg-spinels relative to Cr-, Fe-rich spinels. Given nearly all lunar spinel samples are chromium bearing (up to 55 wt% Cr_2O_3), remotely sensed lunar spinels are expected to also contain above trace levels of chromium.

Chromium in spinel is spectrally active across the visible to near-infrared wavelengths (V-NIR). In general, spinel spectra are characterized by a pair of strong, broad absorptions near 2000 and 2400 nm attributed to Fe^{2+} in tetrahedral coordination

(Figure 1; Cloutis et al., 2004; Jackson et al., 2014). Measureable spectral variations, such as the manifestation of subtle absorptions just short of 1000 nm, reflect variations in Fe# (Fe/(Mg+Fe)*100) and Cr# (Cr/(Cr+Al)*100) of spinel, as discussed below. Chromites, the iron-chromium (octahedral Cr^{3+}) endmember of spinel group minerals, are characterized by increasingly strong absorptions into the visible wavelengths and, in many cases, a distinct feature at 1300 nm attributed to tetrahedral Cr^{2+}(Cloutis et al., 2004).

Laboratory spectroscopic analyses of spinel have also identified a narrow absorption centered at 550 nm (see Figure 1) that has been attributed to octahedral Cr^{3+} in spinel (Mao and Bell, 1975, Cloutis et al., 2004). This 550 nm absorption is commonly weaker than the chromium absorption at 1300 nm, but it has been previously identified in spectra of lunar samples, such as 70002,7 (Mao and Bell, 1975). The strong preference of Cr^{3+} for octahedral crystallographic sites in spinel may influence the ordering of other spectrally active cations in the mineral lattice (Navrotsky and Kleppa, 1967), such as the ratio of octahedral and tetrahedral Fe^{2+}, and thus, may indirectly affect a range of V-NIR spectral properties of spinel. Though the 550 nm feature appears in laboratory spectra of both terrestrial and lunar spinels, it has yet to be identified in the spectra of remotely sensed spinels.

Laboratory studies indicate at FeO contents ≥5 wt%, spectra of synthetic spinels display short wavelength absorption features near 1000 nm related to octahedral Fe^{2+} (Jackson et al., 2014). Low FeO abundances (<5 wt%) are therefore expected for the PSA lithology because remote sensing observations of these regions on the Moon lack observable absorption bands in the 1000 nm spectral range. In contrast, Sinus Aestuum

spinel reflectance spectra display relatively strong absorptions near 600-700, 900-1000, and 1350 nm, suggesting that the Sinus Aestuum spinels are higher in iron and/or chromium abundance than the PSA spinels (Sunshine et al., 2010, 2014; Yamamoto et al., 2013).

The effect of chromium on reflectance properties within the 550-1000 nm spectral range in the absence of abundant Fe^{3+} has not been experimentally studied at lunar oxygen fugacities. The short wavelengths of terrestrial spinel spectra are dominated by the presence of Fe^{3+} absorptions (Cloutis et al., 2004), which should be minimal in lunar samples due to the low lunar fO_2. In this study, we synthesize chromium- and iron-bearing spinels at lunar-like oxygen fugacity (fO_2) in order to determine the influence of chromium content on the spectral characteristics of spinel on the Moon. Identifying the spectral reflectance features of chromium in lunar spinel, as well as constraining the compositions at which the features exist, allows for estimation of the amount of chromium in the spinel-bearing lithologies on the Moon. Our results provide a calibration for interpreting spinel compositions from remote spectral observations and suggest spinels in the PSA lithology have a low Cr#, potentially less than 1.

Methods

Mineral synthesis

Aluminate spinels of varying chromium content were synthesized by mixing approximately stoichiometric proportions of reagent-grade oxide powders (MgO, Fe_2O_3, Al_2O_3, and Cr_2O_3). Oxide powders were homogenized using a mortar and pestle, then

pressed into 1 cm diameter pellets and placed atop zirconia beads all within a low, rectangular alumina crucible. Samples were then sintered in a horizontal gas-mixing furnace for 72 hours at an oxygen fugacity corresponding to 1 log unit below the iron-wüstite buffer at 1450°C.

A series of spinels (CrSp1-8) was synthesized with varying chromium content in order to investigate the effect of chromium on spinel spectra. Eight different starting compositions with Cr# varying from 1 to 29 and a fixed iron content (~5 wt% FeO) were produced to create the CrSp1-8 series. Three additional samples (CrSp9-11) were produced to examine the effect of Fe# and non-stoichiometry on chromium-bearing spinel spectra. Samples CrSp9 and 10 were synthesized following the procedure listed above, but with the aim of fixing chromium content and varying iron content. Sample CrSp11 was produced by adding surplus MgO powder to one of the samples from the CrSp series (CrSp8) and resintering this composition.

Fragments of each synthetic spinel were mounted for electron microprobe analysis, and the remainders were crushed and dry sieved to <45 μm particle size for reflectance spectroscopy and Mössbauer measurements. The <45 μm particle size was chosen in order to provide the most direct analog to remotely sensed lunar spinels, as this particle size fraction dominates the optical properties of lunar soils at V-NIR wavelengths (Pieters et al. 1993; Fischer 1995).

Electron microprobe analysis

Major element compositions of each sample were obtained using the Cameca SX-100 electron microprobe at Brown University. Analyses were performed using 15 kV

accelerating voltage, 20 nA beam current, and a focused beam. Point analyses were spatially distributed throughout the entire sample in order to record any compositional variation.

Mössbauer analysis

All samples were synthesized at the same oxygen fugacity. Mössbauer data obtained at Mount Holyoke determined the coordination state of iron for two of the spinel samples (CrSp3 and 4). The methods outlined in Jackson et al. (2014) are identical for the samples presented in this paper, as the samples were analyzed simultaneously. For a detailed description of the Mössbauer spectroscopy, see Jackson et al. (2014).

Reflectance spectroscopy

Reflectance spectra of our synthetic spinels were acquired in RELAB at Brown University with a spectral resolution ≤5 nm. Dry-sieved samples (<45 μm particle size) were measured by both the Bidirectional Reflectance spectrometer (BDR), which measures V-NIR wavelengths (300-2600 nm), and the Thermo Nicolet Nexus 870 Fourier Transform Infrared spectrometer (FTIR), which measures out to mid-infrared (mid-IR) wavelengths (800-25000 nm). Each BDR and FTIR measurement employed an incidence angle of 30° and emergence angle of 0° (Pieters and Hiroi, 2004). BDR and FTIR data for each sample were spliced near 1000 nm using conventional RELAB procedures in order to smoothly connect the two spectra. All reflectance spectra presented in this paper will be available through the RELAB spectral database

(www.planetary.brown.edu/relab). (RELAB sample directory names are reported in Supplementary Table S1.)

Spectral Analysis

V-NIR band strength is expected to increase with increasing iron and chromium abundance in spinel. To measure this effect on the bands at 550, 1000, 2000, and 2800 nm, the strength of these bands in each sample spectrum was quantified. The spectrum for each sample was first scaled so that the reflectance maximum between 1000–2000 nm (determined by a polynomial fit) equaled one. This procedure minimizes albedo variations among samples to facilitate comparison of band strengths, making a further continuum removal unnecessary. Then, a second-degree polynomial was fit in a least-squares sense between 530-605, 825–1100, 1700–2200, and 2700–3000 nm. The minimum reflectance value for each polynomial was identified, and the natural log of the reflectance minimum [$\ln(\text{reflectance}_{min})$] for each band was calculated. The slope of the correlation between $\ln(\text{reflectance}_{min})$ and the concentration of the cation species responsible for the band is termed the "reflectance coefficient." The reflectance coefficient is used to quantify the relationship between spinel composition and spectral features.

Across the mid-IR spectral range (8000 – 25000 nm or 1250 – 400 cm^{-1}), radiation is commonly measured and reported in terms of emissivity, which can be approximated from our data by subtracting the measured reflectance values from one (Hapke, 1993). We report the mid-IR spectra in this way to facilitate comparison with

previous laboratory studies. The primary spectral features in the mid-IR wavelengths are 1) the Christiansen feature (CF) and 2) the restsrahlen bands (RB). The CF is characterized by a primary emissivity maximum between ~10000 – 11000 nm (~900 – 1000 cm^{-1}) with a secondary CF between ~15000 – 18000 nm (~550 – 650 cm^{-1}) and is diagnostic of mineralogy and bulk composition (Conel, 1969). The RB occur between ~12000 – 15000 nm (~650 – 850 cm^{-1}) and ~15000 – 25000 nm (~400 – 650 cm^{-1}) and represent molecular vibrations related to stretching and bending motions. To determine the wavelength position of these spectral features, a second-degree polynomial was fit to each spectral feature in each spectrum following the approach used to calculate band positions in the V-NIR spectral region. For the CF, a polynomial was fit to a portion of the ~10000 – 11000 nm spectral range of each spectrum and the frequency of the maximum emissivity value in the polynomial fit was used to represent the CF position. The same method was used to find the position of the secondary CF in the ~15000 – 18000 nm spectral range. Diagnostic absorptions in the RB, four in total, were also fit to determine the frequencies of the emissivity minimum values. The spectral range was varied in order to best fit the emissivity and shape of each spectral feature in each sample spectrum. Due to the non-unique nature of identifying the spectral features using this methodology, the positions of spectral features can vary by $\pm$ 20 nm as the spectral range and polynomial order are changed (Donaldson Hanna et al., 2012).

Results

Sample description and major element composition

The experimentally produced samples are porous and contain minor compositional heterogeneities (Figure 2). Table 1 reports the average major element compositions and standard deviations of our synthetic spinels. The predominant phase in our samples is $(Fe,Mg)(Cr,Al)_2O_4$ spinel. For CrSp1-7, Cr# ranges from 1 to 29 with minor variation in iron content (Fe# 8-11). CrSp9 and 10 have similar chromium contents (Cr# 5 and 6, respectively) but vary significantly in iron content (CrSp9 Fe# 21.9, CrSp10 Fe# 30.4), as designed. Within-sample variations of spinel composition are illustrated by the point analyses in Supplemental Table S2. In more Cr-rich samples, excess Cr_2O_3 is present in phases <100 um in diameter (see Figure 2, a-b). Sample CrSp8 (Cr# 14.2) is non-stoichiometric spinel with excess Al_2O_3. Sample CrSp11 (Cr# 14.1) contains minor amounts of periclase (MgO).

Mössbauer spectroscopy

The abundance of Fe^{3+} in spinel is positively correlated to the oxygen fugacity of the system. Mössbauer spectroscopy measured the abundance of Fe^{3+} for samples CrSp3 and 4 (Supplemental Table S3). Measured abundances show that Fe^{3+} comprises 10% and 6% of total iron in samples CrSp3 and CrSp4, respectively. These measurements are consistent with Fe^{3+} abundances (3-14%) in spinels synthesized between IW+1.6 and IW-0.3 by Hålenius et al. (2002), and confirm that reducing conditions were obtained during each of the experimental runs. Because our spinels were synthesized under low fO_2 conditions, our results are relevant to spinel formation on the Moon.

V-NIR spectroscopy

Jackson et al. (2014) have detailed the effect of iron on visible-infrared spectra of synthetic aluminate spinel with emphasis on the 700, 1000, 2000, and 2800 nm absorption bands. The chromium-bearing spinel samples presented have an additional, narrow (~130 nm wide) absorption near 550 nm (Figure 3). The 550 nm band is present in spinels with Cr# as low as 1. Absorption strength increases with increasing chromium content (Figure 4). Our results generate the linear correlation:

$$\ln\left(reflectance_{min}\right) = -0.030 \pm 0.007 \cdot Cr\# - 0.37 \pm 0.08, R^2 = 0.9 \qquad (1)$$

with uncertainties reported in 95% confidence intervals. At the highest chromium concentrations studied, the 550 nm feature appears less sensitive to changes in Cr#. The strength and shape of the characteristic iron absorption features (at 1000, 2000, and 2800 nm) are not affected by the presence of chromium in the experiments. Likewise, iron (Figure 5) and magnesium (Figure 6) have little effect on the 550 nm chromium band, though they exhibit significant effects on longer wavelength bands (Jackson et al., 2014). Each sample spectrum displays a sharp decease in reflectance at wavelengths below 550 nm. This effect is likely related to metal-oxygen charge transfer absorptions associated with iron and chromium cations (Cloutis et al., 2008). When the charge transfer absorptions are removed from the spectra near 550 nm, a relationship between 550 nm feature depth and Cr# remains (Supplementary Figure S3).

MID-IR spectroscopy

Full resolution laboratory emissivity (1 – reflectance) spectra for the CrSp spinel series are plotted across the mid-IR spectral range (8000 – 25000 nm or 1250 – 400 cm^{-1}) in Figure 7. Diagnostic spectral features include the primary Christiansen feature (CF) observed near ~980 cm^{-1} (~10200 nm) and the secondary CF observed near ~620 cm^{-1} (~16100 nm). Mid-IR laboratory spectra show a systematic shift of the primary and secondary CF positions to lower wavenumbers (longer wavelengths) as the Cr# increases (as seen in Figures 7 and 8). Thus, the primary and secondary CF positions can be used to distinguish between compositions of chromium-bearing spinel. The equations fit to the CF positions (wavenumber, cm^{-1}) are as follows:

$$CF1_{pos.} = -2.2 \pm 0.1 \cdot Cr\# + 975 \pm 2, R^2 = 0.996 \quad (2)$$

$$CF2_{pos.} = -0.6 \pm 0.2 \cdot Cr\# + 621 \pm 3, R^2 = 0.873 \quad (3)$$

A similar linear trend is observed between the primary and secondary CF positions and Fe# in emissivity spectra of the olivine solid solution series (Hamilton, 2010) and the synthetic suite of spinels with varying Fe# by Jackson et al. (2014). Four diagnostic absorptions in the reststrahlen band (RB) regions were identified near ~865, 755, 700, and 520 cm^{-1} (~11600, 13200, 14300, and 19200 nm). As seen in Figure 8, the RB near ~860, 760 and 700 cm^{-1} also have linear relationships with Cr# as the diagnostic band positions shift to lower wavenumbers (longer wavelengths), while the position of RB4 near 520 cm^{-1} appears independent of Cr#. The equations fit to the RB positions (wavenumber, cm^{-1}) are as follows:

$$RB1_{pos.} = -1.4 \pm 0.3 \cdot Cr\# + 863 \pm 4, R^2 = 0.958 \quad (4)$$

$$RB2_{pos.} = -2 \pm 2 \cdot Cr\# + 760 \pm 16, R^2 = 0.653 \quad (5)$$

$$RB3_{pos.} = -0.8 \pm 0.3 \cdot Cr\# + 694 \pm 5, R^2 = 0.865 \quad (6)$$

Thus, diagnostic absorption bands in the RB regions can also be used to distinguish between chromium-bearing spinel compositions. Similar trends are observed between RB absorption band positions and Fe# in spinels (Cloutis et al., 2004, Jackson et al., 2014) and olivines (Hamilton, 2010). Uncertainties in regression equations are 95% confidence intervals.

Discussion

Octahedral Cr^{3+} as cause for 550 nm absorption

The correlation between 550 nm band strength and Cr# in our samples, along with previous studies of spinel spectra (Poole, 1964; Mao and Bell, 1975; Cloutis et al., 2004), conclusively link the 550 nm absorption band to octahedral Cr^{3+} in spinel. Tetrahedral Cr^{2+} is known to display an absorption band around 1300 nm (Greskovich and Stubican, 1966; Mao and Bell, 1975; Cloutis et al., 2004). Absence of an absorption band near 1300 nm in our spectral data, combined with spinel stoichiometry from our compositional data, indicates the chromium in our samples is overwhelmingly present as octahedral Cr^{3+}.

Tetrahedral Fe^{2+} within spinel displays strong absorption bands in the near-infrared wavelengths (Cloutis et al., 2004; Jackson et al., 2014), but does not produce the absorption feature at 550 nm observed in our samples. Previous work at similar

synthesis conditions (Jackson et al., 2014) has shown that increasing octahedral Fe^{2+} content increases the strength of the absorption band near 700 nm without giving rise to any absorption bands near 550 nm. Because iron content is held constant for spinels CrSp1-7, the increase in 550 nm band strength could only be due to Fe^{2+} (tetrahedral or octahedral) provided octahedral Cr^{3+} was increasing the proportion of these iron species. The current experiments demonstrate the addition of iron to chromium-bearing spinels does not significantly increase the strength of the 550 nm absorption band (Figure 5). Rather, the iron begins to produce an absorption shoulder near 700 nm. Thus, the 550 nm feature appears to be solely a function of octahedral Cr^{3+}.

Comparison of synthetic spinel to lunar sample 70002,7

Application of our results to remotely gathered data from the Moon requires compositional and spectral similarities between lunar spinels and our synthetic samples. Mao and Bell (1975) report a spectrum from a spinel found in Apollo sample 70002,7, which is compositionally similar to the spinels synthesized in this study (Fe# 11.6 and Cr# 4.29). The spinel spectrum from sample 70002,7 shows absorptions at 1000 and 2000 nm characteristic of Fe^{2+} (Mao and Bell, 1975; Cloutis et al., 2004; Jackson et al., 2014). Additionally, the lunar spinel spectrum shows a narrow absorption band near 550 nm, which the authors attribute to octahedral Cr^{3+}. The 550 nm absorption in the lunar spinel spectrum is similar in strength and depth to the characteristic feature of our synthetic chromium-bearing aluminate spinels (Figure 9). Furthermore, equation (1) predicts Cr# 7 ± 3 from the spinel spectrum of Apollo sample 70002,7, within error of the actual value of 4.3. Thus the experimental calibration can be used to quantify lunar spinel compositions using the strength of the 550 nm spectral feature.

Mid-IR spectral systematics

Extensive data analysis is needed to characterize the mid-IR remote observations of the lunar spinel locations identified by V-NIR techniques (Pieters et al., 2011; Dhingra et al., 2011; Dhingra and Pieters, 2011; Bhattacharya et al., 2012; Kaur et al., 2012; Lal et al., 2012; Yamamoto et al., 2013; Pieters et al., 2014). Our results indicate that the mid-IR spectral range can be used to distinguish chromium-bearing spinel compositions from: (1) one another based on the position of the CF and RB, (2) Mg-spinel compositions with varying Fe#, and (3) silicate minerals found on the lunar surface such as plagioclase, pyroxene, and olivine. As seen in Figure 8, diagnostic spectral features of chromium-bearing spinels systematically shift to lower wavenumbers (longer wavelengths) as the Cr# increases, and importantly, these shifts are relatively large compared to those associated with changes in Fe# (c.f. Jackson et al., 2014). Thus, for locations of pure chromium-bearing spinel on the lunar surface, the CF and RB positions could distinguish the Cr# for that spinel. In addition, the CF and RB positions of chromium-bearing spinel occur at lower wavenumbers (longer wavelengths) that are distinct from the CF and RB positions of silicate minerals such as plagioclase, pyroxene, and olivine. Lunar spinel locations have been identified based on spectra dominated by the aluminate spinel signature, however V-NIR laboratory analysis by Cheek and Pieters (2014) have shown that significant amounts of plagioclase can be mixed into these spinel-rich units before the broad diagnostic absorption band at 1250 nm of plagioclase is observed. Across the mid-IR spectral range, mineral mixtures with rocks and coarse particulates have very high absorption coefficients resulting in few multigrain interactions, and spectral features of the

component minerals add linearly to produce the mixture spectrum (Christensen et al., 1986). Thus, our laboratory mid-IR spectra of chromium-bearing spinels presented here, along with detailed analysis of mid-IR remote observations of lunar spinel locations by the Diviner Lunar Radiometer Experiment onboard NASA's Lunar Reconaissance Orbiter (LRO) and future hyperspectral data sets, could act to better constrain the abundances and compositions of spinel in these spinel-rich areas. In particular, Diviner has three narrow spectral channels near 8000 nm (7810, 8280, and 8550 nm) and one wider spectral channel covering the 12500 – 25000 nm spectral range, which can be used to characterize the wavelength position of the CF and the overall shape of the RB region. These four Diviner spectral channels could be used to easily distinguish between Cr-rich, intermediate-Cr, and Cr-poor spinel compositions, however laboratory emissivity measurements of our synthetic samples under simulated lunar conditions are needed to further refine the degree to which Diviner would be able to distinguish between spinel compositions (e.g., Cr#).

Implications

The connection between a narrow 550 nm absorption band and octahedral Cr^{3+} in the spinel structure provides a tool by which to identify chromium in remotely sensed spinel. Because these experiments were conducted at fO_2 ~IW-1, the results are applicable to any planetary surface with similar redox conditions. Below, we explore the implications of our laboratory investigation for the petrologic interpretation of specific

355 spinel-rich occurrences on the Moon: pink spinel anorthosites in the highlands, and dark
356 mantle deposits at Sinus Aestuum.

357 **Pink Spinel Anorthosite (PSA) lithology**

358 The lack of any observed absorption peak near 550 nm in spectra from both M^3
359 and SP datasets of spinel-bearing lithologies suggests there is little octahedral Cr^{3+} in
360 the remotely sensed spinel, potentially Cr# <1. Spinel in lunar clasts believed to
361 represent the Mg-rich spinel all have Cr# >1 which, by our results, would produce a 550
362 nm absorption feature (Papike et al., 1998; Gross and Treiman, 2011; Treiman and
363 Gross, 2015; Wittman et al., 2015).

364 Assuming the lack of observable 550 nm bands associated with PSA is not a
365 result of other processes, it indicates that the remotely sensed spinels are very Cr-poor
366 and Al-rich. Highly aluminate spinels are typically associated with Mg-suite materials
367 and can be produced by assimilation of plagioclase-rich lunar crust by Mg-suite parental
368 magmas (Prissel et al., 2014). The petrology of the Mg-suite rocks indicates their
369 parental magmas contained high normative abundances of plagioclase and were
370 relatively Cr-poor (Elardo et al., 2011), providing a link between Mg-suite magmatism
371 and PSA observations. This link is strengthened by the low Fe# associated with the Mg-
372 suite parental magmas and PSA spinel (Jackson et al., 2014). Thus, PSA lithologies
373 plausibly represent locations where substantial amounts of crustal material were
374 assimilated into Mg-suite magmas. Alternatively, the Cr-poor and Al-rich spinel
375 composition could be produced from hybridized mantle melts (Longhi et al., 2010) or
376 impact melting (Gross et al., 2014).

Dark Mantle Deposits at Sinus Aestuum

Spectral data on pyroclastic deposits at Sinus Aestuum contain a "visible feature" around 600-700 nm (Sunshine et al., 2010, 2014; Yamamoto et al., 2013), but no obvious absorptions at shorter wavelengths. The 600-700 nm band center is clearly offset from band centers related to octahedral Cr^{3+}, a fundamental cation species required to stabilize chromite components within spinel. Thus, our results argue against previous suggestions that the Dark Mantle Deposits at Sinus Aestuum contain large chromite components because the characteristic octahedral Cr^{3+} spinel absorption is absent (Sunshine et al., 2010, 2014; Yamamoto et al., 2013).

Rather, we suggest that the spinels observed at Sinus Aestuum are dominantly aluminate spinels that are distinctly more Fe-rich compared to the remaining remote observations of PSA spinels. This suggestion is in accordance with previous interpretations of the Sinus Aestuum spinel spectra (Yamamoto et al., 2013), as well as the Fe-rich (>16 wt% FeO) pyroclastic glasses returned from the Moon (e.g. Delano, 1986). However, Cr-rich spinels are expected to form during typical mare basalt or lunar picritic liquid crystallization (Elkins-Tanton et al., 2003). In order to stabilize low Cr# spinels, we suggest the pyroclastic materials at Sinus Aestuum assimilated a relatively large amount of plagioclase, similar to the model proposed for PSA (above), leading to a decreased Cr# prior to eruption. Again, this suggests that Sinus Aestuum region experienced a relatively protracted magmatic history with multiple pulses of magmatism, as these conditions favor assimilation of country rock.

Select spectra at Sinus Aestuum are reported to exhibit a 1300 nm absorption band (Yamamoto et al., 2013), and this band has been attributed to tetrahedral Cr^{2+} (Cloutis et al., 2004). It is possible that tetrahedral Cr^{2+} is present in the Sinus Aestuum spinels, but given the lack of evidence for octahedral Cr^{3+}, the affinity of spinel for octahedral Cr^{3+}, and the observation of abundant octahedral Cr^{3+} in lunar spinels (Haggerty, 1971, 1972, 1973, 1977), this would imply an extremely reduced oxygen fugacity for the Sinus Aestuum pyroclastic materials.

Alternative explanations for the lack of an observed 550 nm absorption could include that (1) the remote detection limits are very high (perhaps related to the decreased signal/noise ratio of M^3 and SP at short wavelengths), (2) space weathering has preferentially muted the 550 nm band, or (3) mixing with other materials has preferentially muted the 550 nm band. Gross et al. (2015) demonstrated that the Cr^{3+} absorption near 550 nm remains robust after simulated space weathering, indicating that space weathering is not a likely cause for the lack of 550 nm bands in remotely sensed lunar spinels. Further, laboratory spectra taken of spinel-plagioclase mixtures demonstrate that the 550 nm band for a spinel with Cr# 0.1 is detectable in laboratory settings, even at low spinel abundance (~15 vol%) (Cheek and Pieters, 2014). V-NIR and thermal mixture modeling, combined with thorough analysis of M3 and SP signal/noise ratios at short wavelengths, should help to refine this constraint. Future work to determine the effect of lower oxygen fugacity, higher chromium contents, and space weathering across a range of wavelengths will improve compositional constraints based on the 550 nm feature.

Acknowledgements:

The authors thank Taki Hiroi for assistance with spectral measurements and Joseph Boesenberg for assistance with EMP measurements. We thank E.A. Cloutis and S. Yamamoto for their thoughtful reviews of the manuscript. Additional thanks go to Reid F. Cooper who assisted in the early stages of this project. Support for this work was provided through NLSI (NNA09DB34A) and SSERVI (NNA13AB014).

References:

Bhattacharya, S., Chauhan, P., and Ajai [no initial] (2012) Discovery of orthopyroxene-olivine-spinel assemblage from the lunar nearside using Chandrayaan-1 Moon Mineralogy Mapper data. Current Science, 103, 21–23.

Bhattacharya, S., Saran, S., Dagar, A. Chauhan, P., Chauhan, M., Ajai [no initial], and Kumar, A.S.K. (2013) Endogenic water on the Moon associated with non-mare silicic volcanism: implications for hydrated lunar interior. Current Science, 105, 685–691.

Cheek, L.C., and Pieters, C.M. (2014) Reflectance spectroscopy of plagioclase and mafic mineral mixtures: Implications for characterizing lunar anorthosites remotely. American Mineralogist, 99, 1871–1892.

Christensen, P. R. (1986) The spatial distribution of rocks on Mars. Icarus, 68, 217-238.

Cloutis, E.A., Sunshine, J.M., and Morris, R.V. (2004) Spectral reflectance-

compositional properties of spinels and chromites: Implications for planetary remote sensing and geothermometry. Meteoritics & Planetary Science, 39, 545–565.

Cloutis, E.A., McCormack, K.A., Bell, J.F. III, Hendrix, A.R., Bailey, D.T., Craig, M.A., Mertzman, S.A., Robinson, M.S., and Riner, M.A. (2008) Ultraviolet spectral reflectance properties of common planetary minerals. Icarus, 197, 321-347.

Conel, J. E. (1969) Infrared emissivities of silicates: Experimental results and a cloudy atmospheric model of spectral emission from condensed particulate mediums. Journal of Geophysical Research, 74, 1614-1634.

Delano, J.W., (1986) Pristine Lunar Glasses: Criteria, Data, and Implications. Journal of Geophysical Research, 91, B4, D201 – D213.

Dhingra, D., and Pieters, C.M. (2011) Mg-Spinel rich lithology at crater Copernicus. Annual Meeting of the Lunar Exploration Analysis Group, 2024.

Dhingra, D., Pieters, C.M., Boardman, J., Head, J.W. III, Isaacson, P.J., Taylor, L.A., and M3 Team (2011a) Theophilus Crater: Compositional diversity and geological context of Mg-spinel bearing central peaks. Lunar and Planetary Science Conference, 42, 2388.

Dhingra, D., Pieters, C.M., Boardman, J.W., Head, J.W., Isaacson, P.J., and Taylor, L.A. (2011b) Compositional diversity at Theophilus crater: Understanding the geologic context of Mg-spinel bearing central peaks. Geophysical Research Letters, 38, L11201.

461 Donaldson Hanna, K. L., I. R. Thomas, N. E. Bowles, B. T. Greenhagen, C. M. Pieters,
462 J. F. Mustard, C. R. M. Jackson, and M. B. Wyatt (2012) Laboratory emissivity
463 measurements of the plagioclase solid solution series under varying environmental
464 conditions, Journal Geophysical Research, 117, E11, doi:10.1029/2012JE004184.

465 Donaldson Hanna, K. (2013) Compositional diversity of the Moon's anorthositic crust:
466 Integrating remote observations with laboratory measurements of analog materials
467 under simulated lunar conditions, p. 306. Ph.D. thesis, Brown University, Providence,
468 Rhode Island.

469 Elardo, S.M., Draper, D.S., and Shearer, C.K. Jr. (2011) Lunar Magma Ocean
470 crystallization revisited: Bulk composition, early cumulate mineralogy, and the source
471 regions of the highlands Mg-suite. Geochimica et Cosmochimica Acta, 75, 3024–3045.

472 Elkins-Tanton, L.T., Chatterjee, N., and Grove, T.L. (2003) Experimental and
473 petrological constraints on lunar differentiation from the Apollo 15 green picritic glasses.
474 Meteoritics and Planetary Science, 38, 515-527.

475 Fischer, E.M. (1995) Quantitative compositional analysis of the lunar surface from
476 reflectance spectroscopy: Iron, aluminum, and a model for removing the optical effects
477 of space weathering. Ph.D. dissertation, Brown University, Providence, Rhode Island.

478 Greskovich G. and Stubican V. S. 1966. Divalent chromium in magnesium-chromium
479 spinels. Journal of Physics and Chemistry of Solids 27:1379–1384.

480 Gross, J., and Treiman, A.H. (2011) Unique spinel-rich lithology in lunar meteorite ALHA
481 81005: Origin and possible connection to M3 observations of the far- side highlands.

Journal of Geophysical Research, 116, E10009, http://dx.doi.org/10.1029/2011JE003858.

Gross, J., Isaacson, P.J., Treiman, A.H., Le, L., and Gorman, J.K. (2014) Spinel-rich lithologies in the lunar highland crust: Linking lunar samples with crystallization experiments and remote sensing. American Mineralogist, 99, 1849-1859.

Gross, L., Gillis-Davis, J., Isaacson, P.J., and Le, L. (2015) How rich is rich? Placing constraints on the abundance of spinel in the pink spinel anorthosite lithology on the Moon through space weathering. Lunar and Planetary Science Conference, 46, 2642.

Haggerty, S.E., 1971. Compositional variations in lunar spinels. Nature, 233 (43), 156–160.

Haggerty, S.E., 1972. Apollo 14: subsolidus reduction and compositional variations of spinels. In: 3rd Lunar Science Conference Proceedings, 1, pp. 305–332.

Haggerty, S.E., 1973. Luna 20: mineral chemistry of spinel, pleonaste, chromite, ul-vo spinel, ilmenite and rutile. Geochimica et Cosmochimica Acta, 37 (4), 857–867.

Haggerty, S.E., 1977. Luna 24: opaque mineral chemistry of gabbroic and basaltic fragments from mare crisium. Geophysical Reserach Letters, 4 (10), 489–492.

Hålenius, U., Skogby, H., and Andreozzi, G.B. (2002) Influence of cation distribution on the optical absorption spectra of Fe3+-bearing spinel s.s. hercynite crystals: evidence for electron transitions in VIFe2+–VIFe3+ clusters. Physics and Chemistry of Minerals, 29, 39–330.

Hamilton, V. E. (2010) Thermal infrared (vibrational) spectroscopy of Mg-Fe olivines: A review and applications to determining the composition of planetary surfaces. Chemie der Erde, 70, 7-33

Hapke, B. (1993) Theory of Reflectance and Emittance Spectroscopy, Cambridge University Press, New York.

Jackson, C.R.M., Cheek, L.C., Williams, K.B., Donaldson Hanna, K., Pieters, C.M., Parman S.W., Cooper, R.F., Dyar, M.D., Nelms, M., and Salvatore, M.R. (2014) Visible-infrared spectral properties of iron-bearing aluminate spinel under lunar-like redox conditions. American Mineralogist, 99, 1821–1833.

Kaur, P., Chauhan, P., Bhattacharya, S., Ajai [no intial], and Kumar, A.S.K. (2012) Compositional diversity at Tycho Crater: Mg-spinel exposures detected from Moon Mineralogical Mapper (M3) data. Lunar and Planetary Science Conference, 43, 1434.

Kaur, P., Chauhan, P., and Ajai [no initial] (2013a) Detection of Mg-spinel exposures from the anorthositic terrain surrounding Mare Ingenii on the far side of the Moon. Lunar and Planetary Science Conference, 44, 1547.

Kaur, P., Chauhan, P., and Ajai [no initial] (2013b) Exposures of Mg-spinel on an evolved silicic lithology Hansteen Alpha on the Moon. Lunar and Planetary Science Conference, 44, 1348.

Kaur, P., and Chauhan, P. (2014) Detection of spinels exposures from some near side locations of the Moon. Lunar and Planetary Science Conference, 45, 2059.

Lal, D., Chauhan, P., Shah, R.D., Bhattacharya, S., Ajai [no initial], and Kumar, A.S.K.

(2011) Identification of spinel group of minerals on central peak of crater Theophilus. Lunar and Planetary Science Conference, 42, 1339.

Lal, D., Chauhan, P., Shah, R.D., Bhattacharya, S., Ajai [no initial], and Kirankumar, A.S. (2012) Detection of Mg spinel lithologies on central peak of crater Theophilus using Moon Mineralogy Mapper (M3) data from Chandrayaan-1. Journal of Earth System Science, 121, 847–853.

Longhi, J., Durand, S.R., and Walker, D. 2010. The pattern of Ni and Co abundances in lunar olivines. Geochimica et Cosmochimica Acta, 74, 784 - 798.

Mao, H.K., and Bell, P.M. (1975) Crystal-field effects in spinel: oxidation states of iron and chromium. Geochimica et Cosmochimica Acta, 39, 865–866, IN1–IN2, 867–874.

Navrotsky, A., and Kleppa, O.J. (1967) Thermodynamics of cation distributions in simple spinels. Journal of Inorganic & Nuclear Chemistry, 29, 2701–2714.

Papike, J.J., Ryder, G., and Shearer, C.K. Jr. (1998) Lunar Samples. Reviews in Mineralogy and Geochemistry, 36, 5.1-5.234.

Pieters, C.M., Fischer, E.M., Rode, O., and Basu, A. (1993) Optical effects of space weathering: The role of the finest fraction. Journal of Geophysical Research, 98, 20817–20824.

Pieters, C.M., and T. Hiroi (2004) RELAB (Reflectance Experiment Laboratory): A NASA Multiuser Spectroscopy Facility. Lunar and Planetary Science Conference, 35, Abstract 1720.

Pieters, C.M., Boardman, J., Buratti, B., Clark, R., Combe, J.-P., Green, R., Goswami, J. N., Head, J.W. III, Hicks, M., Isaacson, P., and others. (2010) Identification of a new spinel-rich lunar rock type by the Moon Mineralogy Mapper (M3). Lunar and Planetary Science Conference, 41, 1854.

Pieters, C.M., Besse, S., Boardman, J., Buratti, B., Cheek, L., Clark, R.N., Combe, J.P., Dhingra, D., Goswami, J.N., Green, R.O., and others. (2011) Mg-spinel lithology: A new rock type on the lunar farside. Journal of Geophysical Research-Planets, 116, E00G08.

Pieters C.M., Donaldson Hanna, K., Cheek, L., Dhingra, D., Moriarty, D., Parman, S., Jackson, C., and Prissel, T. (2013) Compositional Evolution of the early lunar crust: Observed diverse mineralogy of the upper and lower crust. Lunar and Planetary Science Conference, 44, 2545.

Pieters, C.M., Donaldson-Hanna, K., Cheek, L., Dhingra, D., Prissel, T., Jackson, C., Moriarty, D., Parman, S., and Taylor, L.A. (2014) The distribution of Mg-spinel across the Moon and constraints on crustal origin. American Mineralogist, 99, 1893–1910.

Poole C. P. 1964. The optical spectra and color of chromium containing solids. Journal of Physics and Chemistry of Solids 25: 1169–1182.

Prissel, T.C., Parman, S.W. Jackson, C.R., Rutherford, M.J., Hess, P.C., Head, J.W., Cheek, L., Dhingra, D., and Pieters, C.M. (2014) Pink Moon: The petrogenesis of pink spinel anorthosites and implications concerning Mg-suite magmatism. Earth and Planetary Science Letters, 403, 144–156, http://dx.doi.org/10.1016/j. epsl.2014.06.027.

Sun, Y., Lin, L., and Zhang, Y.Z. (2013) Detection of Mg-spinel bearing central peaks

using M3 images. Lunar and Planetary Science Conference, 44, 1393.

Sunshine, J., Besse, S., Petro, N., Pieters, C., Head, J., Taylor, L., Klima, R., Isaacson, P., Boardman, J., and Clark, R. (2010) Hidden in plain sight: Spinel-rich deposits on the nearside of the Moon as revealed by Moon Mineralogy Mapper (M3). Lunar and Planetary Science Conference, 41, Abstract 1508.

Sunshine, J., Petro, N., Besse, S., Gaddis, L.R. (2014) Widespread Exposures of Small Scale Spinel-Rich Pyroclastic Deposits in Sinus Aestuum. Lunar and Planetary Science Conference, 45, Abstract 1777.

Taylor, L.A., and Pieters, C.M. (2013) Pink-spinel anorthosite formation: Considerations for a feasible petrogenesis. Lunar and Planetary Science Conference, 44, 2785.

Treiman, A.H., and Gross, J. (2015) A rock fragment related to the magnesian suite in lunar meteorite Allan Hills (ALHA) 81005. American Mineralogist, 100, 414-426.

Wittman, A., Korotev, R.L., and Jolliff, B.L. (2015) Lunar Mantle Spinel in Dhofar 1528? Lunar and Planetary Science Conference, 46, 1832.

Yamamoto, S., Nakamura, R., Matsunaga, T., Ogawa, Y., Ishihara, Y., Morota, T., Hirata, N., Ohtake, M., Hiroi, T., and Yokota, Y. (2013) A new type of pyroclastic deposit on the Moon containing Fe-spinel and chromite. Geophysical Research Letters, 40, 4549–4554.

584 **Figure captions:**

585

586 **Figure 1**, V-NIR spectra of terrestrial and lunar chromium-bearing spinels. Note the
587 strong, broad, characteristic spinel absorptions near 2000 and 2400 nm. Terrestrial
588 samples S117, S124, and S125 (Cloutis et al., 2004) illustrate the effect of Fe_2O_3 on
589 spinel spectra, most notably in shorter wavelengths (<1200 nm). In comparison, the
590 spinel spectrum from lunar sample 70002,7 (Mao and Bell, 1975) exhibits a prominent
591 band only at 550 nm in the shorter wavelengths and is substantially brighter between
592 600 and 1000 nm. The sharp 550 nm feature also appears in the terrestrial spectra -
593 though slightly muted - and is here attributed to octahedral Cr^{3+}. Figure legend identifies
594 sample name and oxide weight percent (wt%) for species of interest. Spectral
595 reflectance scaled as described in text.

596

597 **Figure 2**, Back-scattered electron (BSE) images showing minor heterogeneity of
598 experimental products. **a)** Porous CrSp3 grain: light grey represents spinel phase; bright
599 spots caused by excess Cr_2O_3. **b)** Enlarged BSE image of CrSp3 (image area is
600 highlighted by the inset in **a)**. **c)** CrSp2: light grey represents spinel phase. **d)** CrSp11:
601 dark grey grain portions at top of image are periclase (MgO).

602 **Figure 3**, V-NIR spectra of CrSp1-7 (<45 μm grain size) with ~ 5 wt % FeO. All samples
603 display a relatively narrow band centered near 550 nm associated with octahedral Cr^{3+}.
604 Separate bands centered at 1000, 2000, and 2800 nm are also present and associated

with Fe. Figure legend identifies sample name and Cr#. Spectral reflectance scaled as described in text. Unscaled spectra plot available in supplement.

Figure 4, Correlation between ln(reflectance$_{min}$) for the 550 nm band and Cr# at <45 μm particle size for samples. The ln(reflectance$_{min}$) parameter is inversely proportional to band strength. Values of ln(reflectance$_{min}$) for the 550 nm band correlate linearly with Cr# [slope = -0.030 ± 0.007 (95% confidence), r^2 = 0.9], but the regression does not pass through the origin [intercept = -0.37 ± 0.08 (95% confidence)]. This likely reflects a small amount of darkening local to the 550 nm region related to other absorbing species.

Figure 5, Effect of Fe on V-NIR spectra of chromium-bearing spinel: Samples CrSp5, CrSp9, and CrSp10 show the V-NIR spectral effects of increasing bulk Fe content on samples with Cr# ~ 5. Figure legend identifies sample name, Cr#, and Fe#. Spectral reflectance scaled as described in text. Unscaled spectra plot available in supplement.

Figure 6, Effect of MgO-rich non-stoichiometry on V-NIR spectra: Sample CrSp11 (solid spectrum) was prepared by adding an additional 4.1 wt % MgO to the starting oxides of CrSp8 (dashed spectrum). The addition of MgO shifts the non-stoichiometry of the spinel away from excess Al_2O_3. Sample CrSp11 has severely weakened 2000

and 2800 nm bands but a strengthened 1000 nm band compared to CrSp8. Spectral reflectance scaled as described in text.

Figure 7, Mid-IR spectra from select samples (<45 μm grain size). Spectra are offset for clarity and vertical lines highlight the positions of identified features. The primary Christiansen feature is near ~980 cm^{-1} (~10200 nm) and the secondary CF is near ~620 cm^{-1} (~16100 nm). Reststrahlen band regions are located near ~865, 755, 700, and 520 cm^{-1} (~11600, 13200, 14300, and 19200 nm). The spectral contrast in the mid-IR spectrum for CrSp5 is anomalous compared to the other mid-IR spectra of the CrSp series but the mid-IR CF and RB feature positions are consistent with the remaining spectra.

Figure 8, Mid-IR spectral systematics from the CrSp series (<45 μm grain size). The positions of Christiansen features 1 (a) and 2 (b) are negatively correlated to Cr#. Four reststrahlen bands are identified (Absorptions 1-4, c-f). The positions of Absorption 1, 2 and 3 are negatively correlated to Cr#. The position of Absorption 4 appears independent of Cr#.

Figure 9, Sample spectra (CrSp5 and CrSp9) comparison with spectra of spinel in Apollo sample 70002,7 from Mao and Bell (1975). Figure legend identifies sample name, Cr#, and Fe#. The 550 nm band shape in the lunar spinel spectrum is identical to

that of our synthetic analogs, and all three samples contain roughly the same amount chromium. Spectral reflectance scaled as described in text.

Supplementary Figure Captions

Figure S1, V-NIR spectra of CrSp1-7 (<45 μm grain size) with ~ 5 wt % FeO. All samples display a relatively narrow band centered near 550 nm associated with octahedral Cr^{3+}. Separate bands centered at 1000, 2000, and 2800 nm are also present and associated with Fe. Figure legend identifies sample name and Cr#.

Figure S2, Effect of Fe on V-NIR spectra of chromium-bearing spinel: Samples CrSp5, CrSp9, and CrSp10 show the V-NIR spectral effects of increasing bulk Fe content on samples with Cr# ~ 5. Figure legend identifies sample name, Cr#, and Fe#.

Figure S3, Continuum-removed V-NIR spectra (a) of CrSp1-7 (<45 μm grain size) with ~ 5 wt% FeO. A continuum fit between 500 nm and 650 nm was removed to isolate the 550 nm feature from the short-wavelength steepening observed in the original spectra. The resulting correlation between $\ln(\text{reflectance}_{min})$ for the 550 nm band and Cr# differs from the original regression line, but maintains that the $\ln(\text{reflectance}_{min})$ parameter is inversely proportional to band strength [-0.0075 Cr# + 0.8621, $r^2 = 0.9$].

Table 1. Averaged compositions of experimental starting materials reported in wt% oxides.

	n[a]	SiO_2	S.D.	TiO_2	S.D.	Al_2O_3	S.D.	Cr_2O_3	S.D.	FeO[b]	S.D.	MnO	S.D.	MgO	S.D.	CaO	S.D.	NiO	S.D.	Total	S.D.
CrSp1	9	--		--		68	1	1	1	5	2	--		26	1	--		--		100	2
CrSp2	6	--		--		67	2	3.1	7	5.5	2	--		25.2	5	--		--		100	2
CrSp3	7	0.08	6	--		67	1	3	1	4	1	--		25	1	n.a.		--		99.7	7
CrSp4	6	0.1	5	--		67	2	4	1	4	1	--		24.6	8	n.a.		--		100	1
CrSp5	9	0.12	3	--		64	4	5	3	5.1	3	--		25.0	9	--		--		99	2
CrSp6	11	0.09	6	--		50	5	21	4	4.5	3	--		23.7	9	--		--		100	2
CrSp7	8	0.2	1	--		45	3	27	3	5.0	3	0.08	2	22.9	4	n.a.		--		100	1
CrSp8	5	--		--		58.2	6	14	1	5.0	4	0.05	3	21.9	8	n.a.		--		100	3
CrSp9	9	--		--		63	2	5	2	10.9	3	--		21.7	3	n.a.		--		101.1	8
CrSp10	10	--		--		62	2	5	2	14.5	2	--		18.5	7	--		--		100	2
CrSp11	10	0.16	2	--		56.9	7	13.9	6	2.7	6	--		26.0	4	--		0.05	4	100	1

Note : **S.D.** denotes 2σ standard deviation on the last significant digit reported. Cr# = [Cr/(Cr + Al)] x 100; Fe# = [Fe/(Fe + Mg)] x 100. Analyses below detectab

[a] Number of analyses.

[b] FeO = total iron.

Cr#	S.D.	Fe#	S.D.
1	1	11	4
3.0	7	10.9	2
3	1	8	3
4	1	9	2
5	4	10.2	8
22	5	9.6	8
29	4	11.0	6
14.2	9	11.3	5
6	2	21.9	6
5	2	30.4	8
14.1	6	5	1

le limits denoted by "--". n.a. = not analyzed.

Figure 1

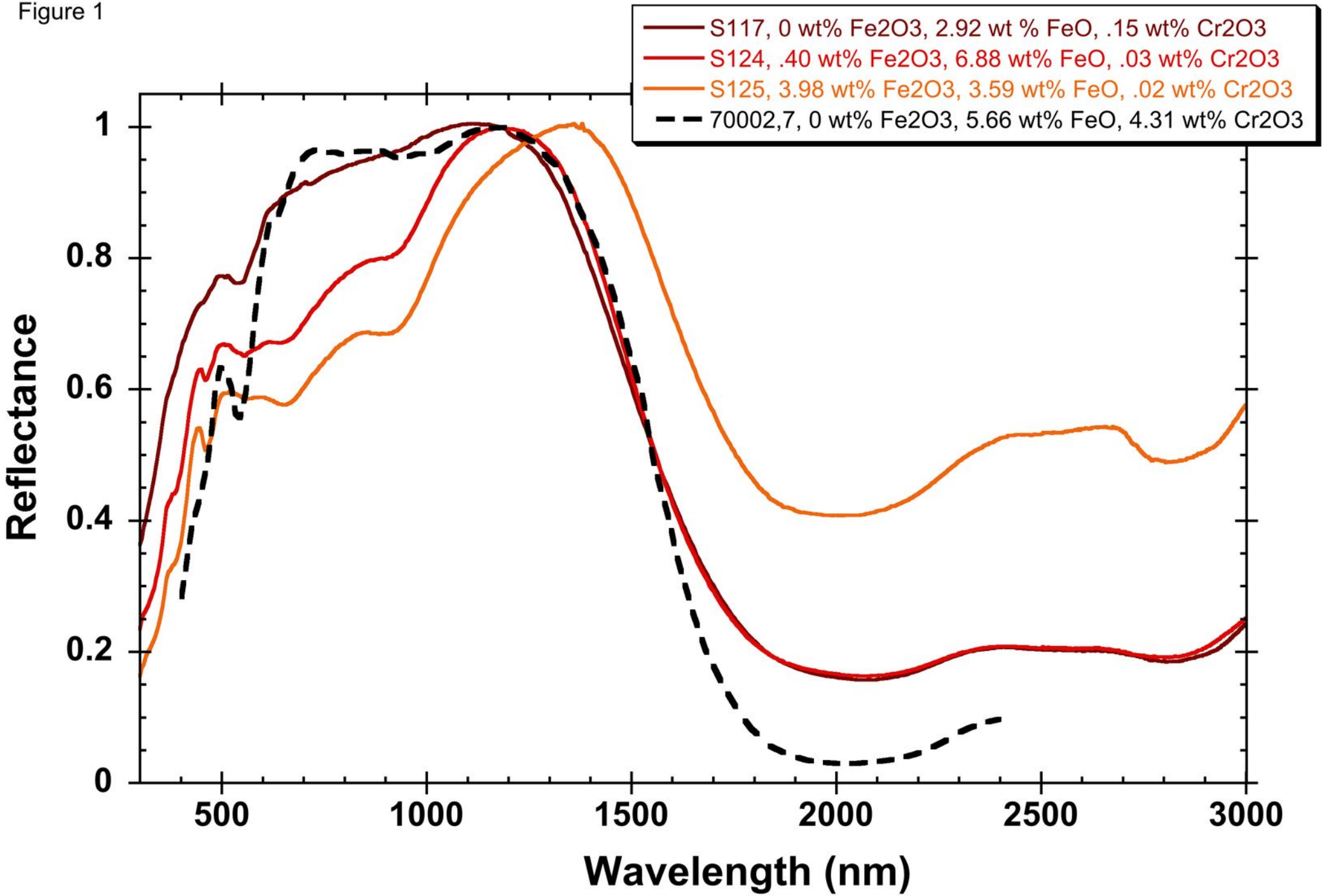
S117, 0 wt% Fe2O3, 2.92 wt % FeO, .15 wt% Cr2O3
S124, .40 wt% Fe2O3, 6.88 wt% FeO, .03 wt% Cr2O3
S125, 3.98 wt% Fe2O3, 3.59 wt% FeO, .02 wt% Cr2O3
70002,7, 0 wt% Fe2O3, 5.66 wt% FeO, 4.31 wt% Cr2O3
Reflectance
0
0.2
0.4
0.6
0.8
1
500
1000
1500
2000
2500
3000
Wavelength (nm)

Figure 2

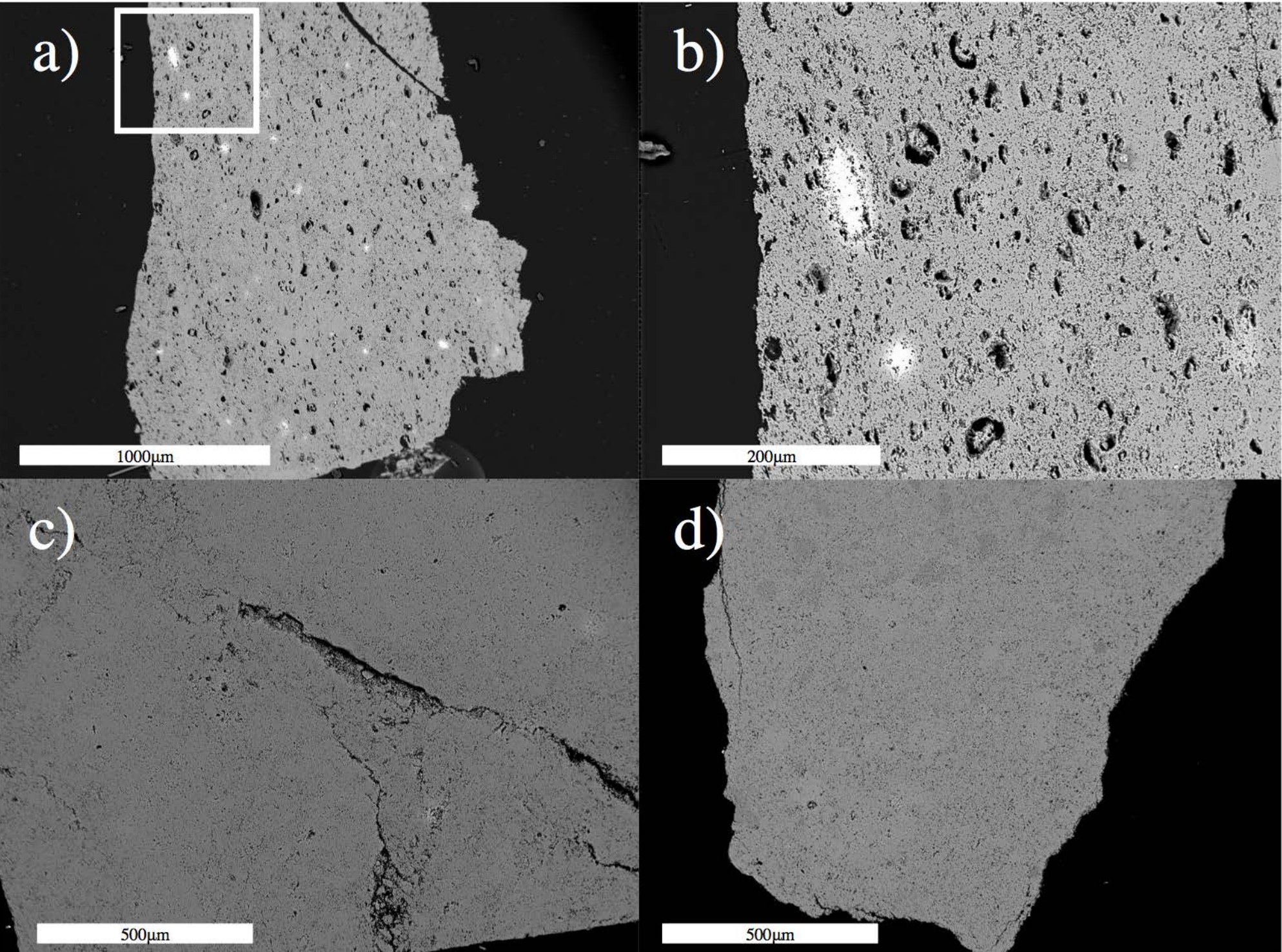

Figure 3

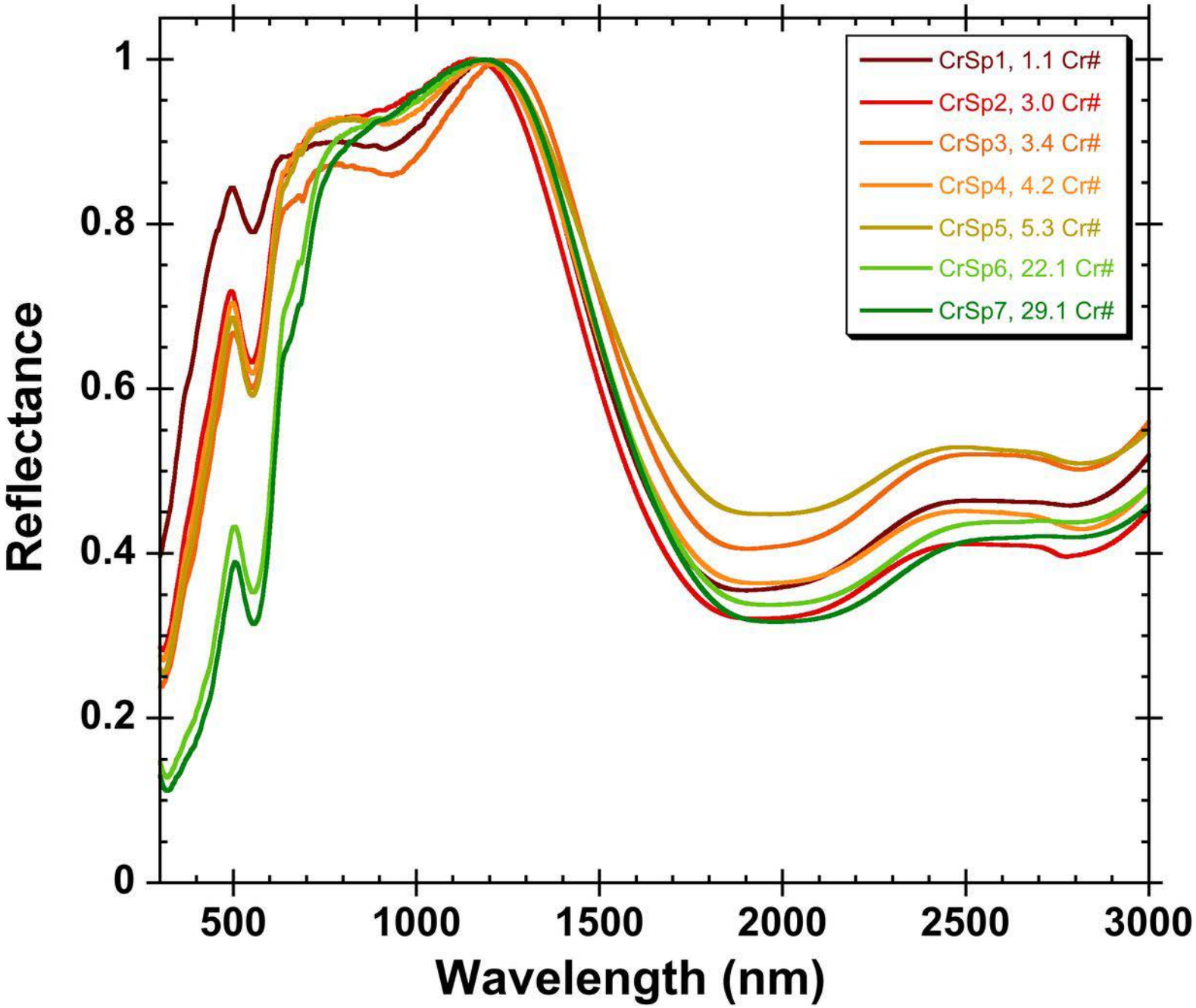
CrSp1, 1.1 Cr#
CrSp2, 3.0 Cr#
CrSp3, 3.4 Cr#
CrSp4, 4.2 Cr#
CrSp5, 5.3 Cr#
CrSp6, 22.1 Cr#
CrSp7, 29.1 Cr#
Reflectance
0
0.2
0.4
0.6
0.8
1
500
1000
1500
2000
2500
3000
Wavelength (nm)

Figure 4

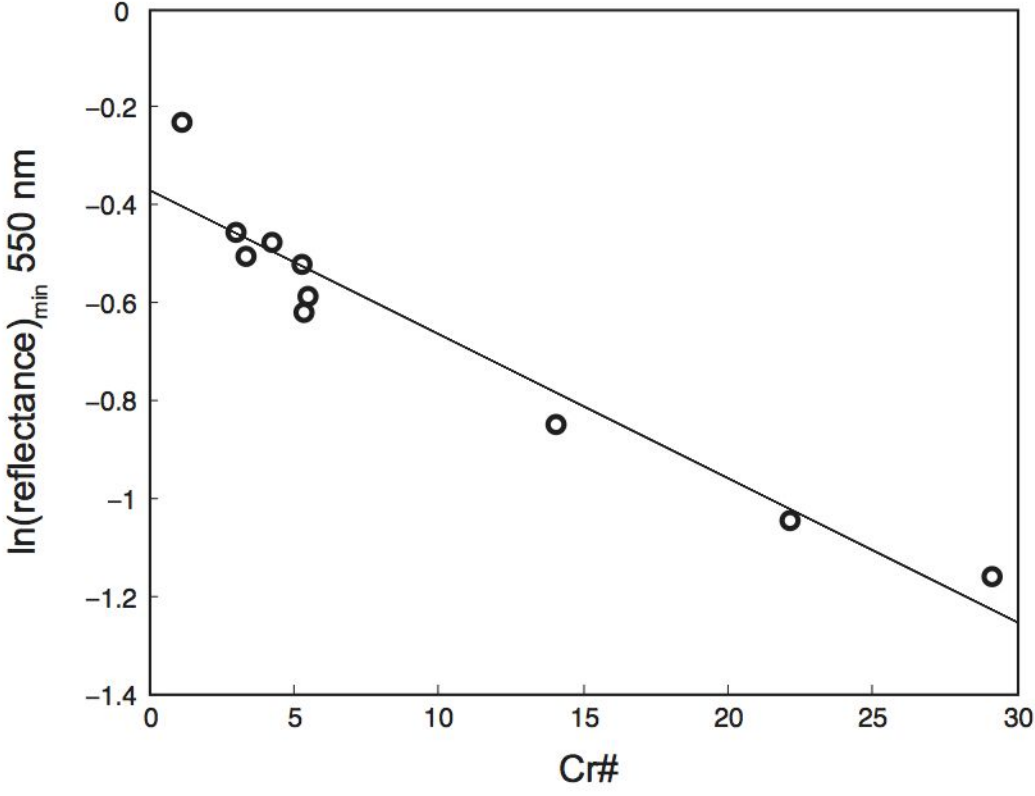

Figure 5

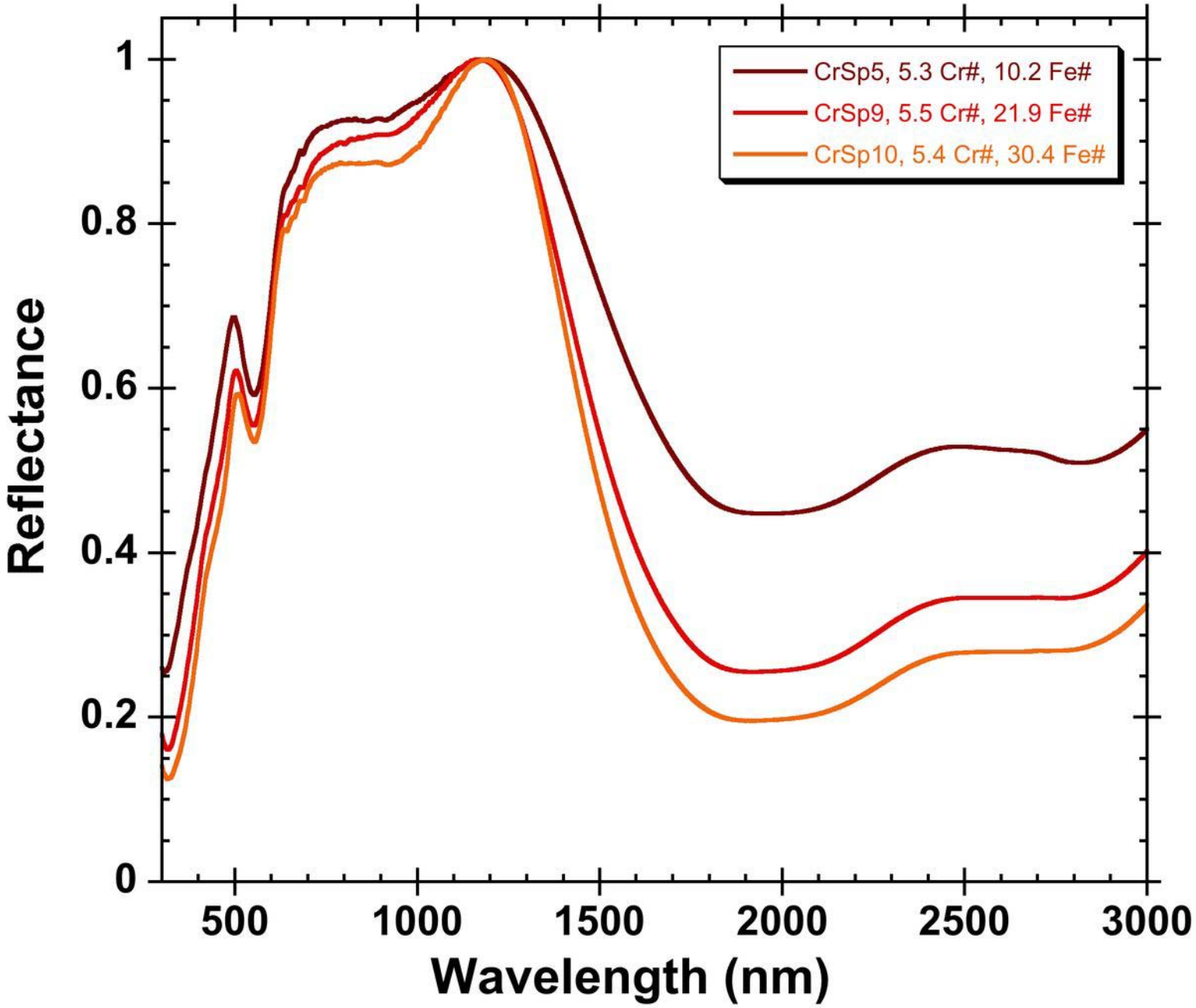
CrSp5, 5.3 Cr#, 10.2 Fe#
CrSp9, 5.5 Cr#, 21.9 Fe#
CrSp10, 5.4 Cr#, 30.4 Fe#
Reflectance
0
0.2
0.4
0.6
0.8
1
500
1000
1500
2000
2500
3000
Wavelength (nm)

Figure 6

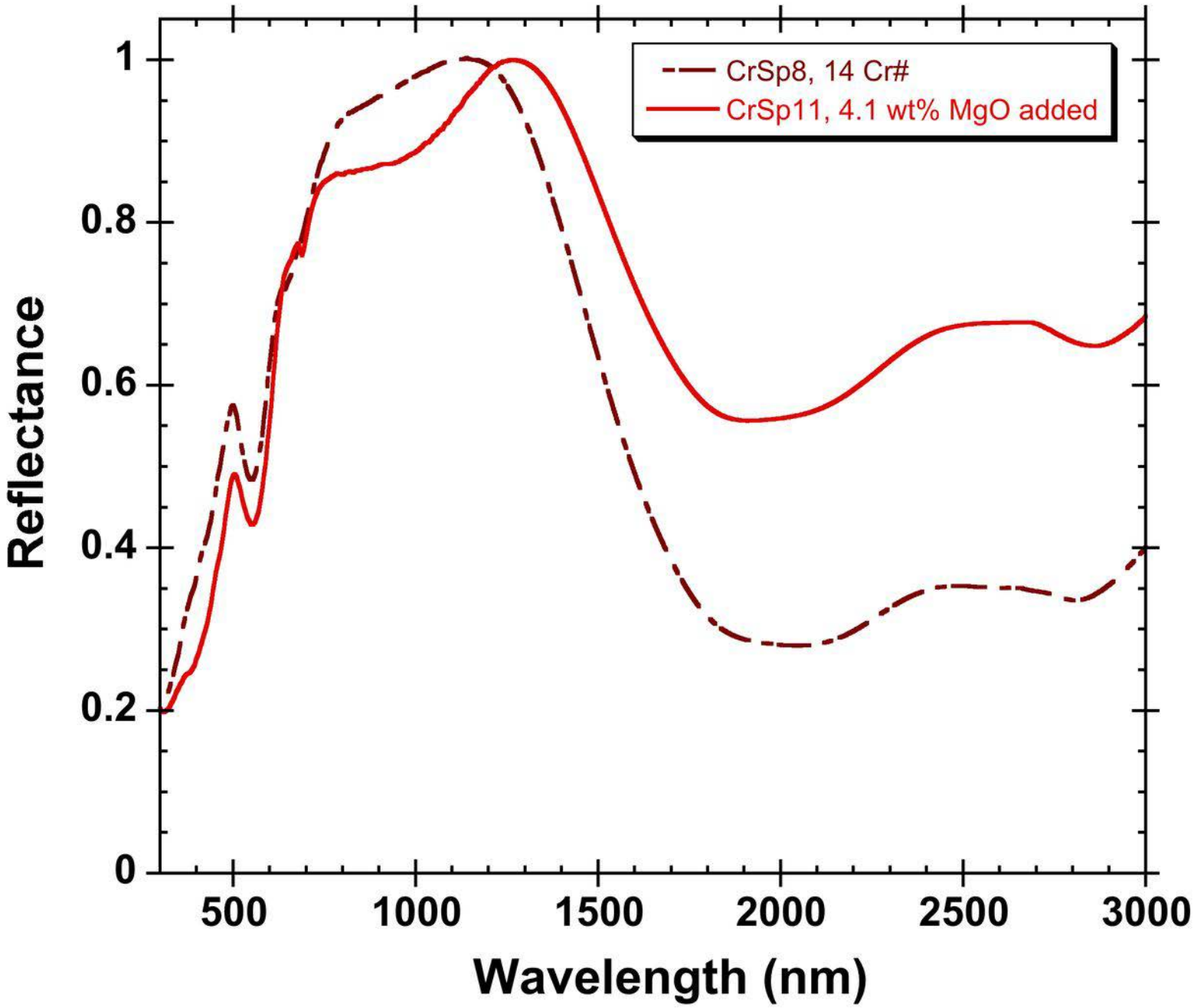
CrSp8, 14 Cr#
CrSp11, 4.1 wt% MgO added
Reflectance
0
0.2
0.4
0.6
0.8
1
500
1000
1500
2000
2500
3000
Wavelength (nm)

Figure 7

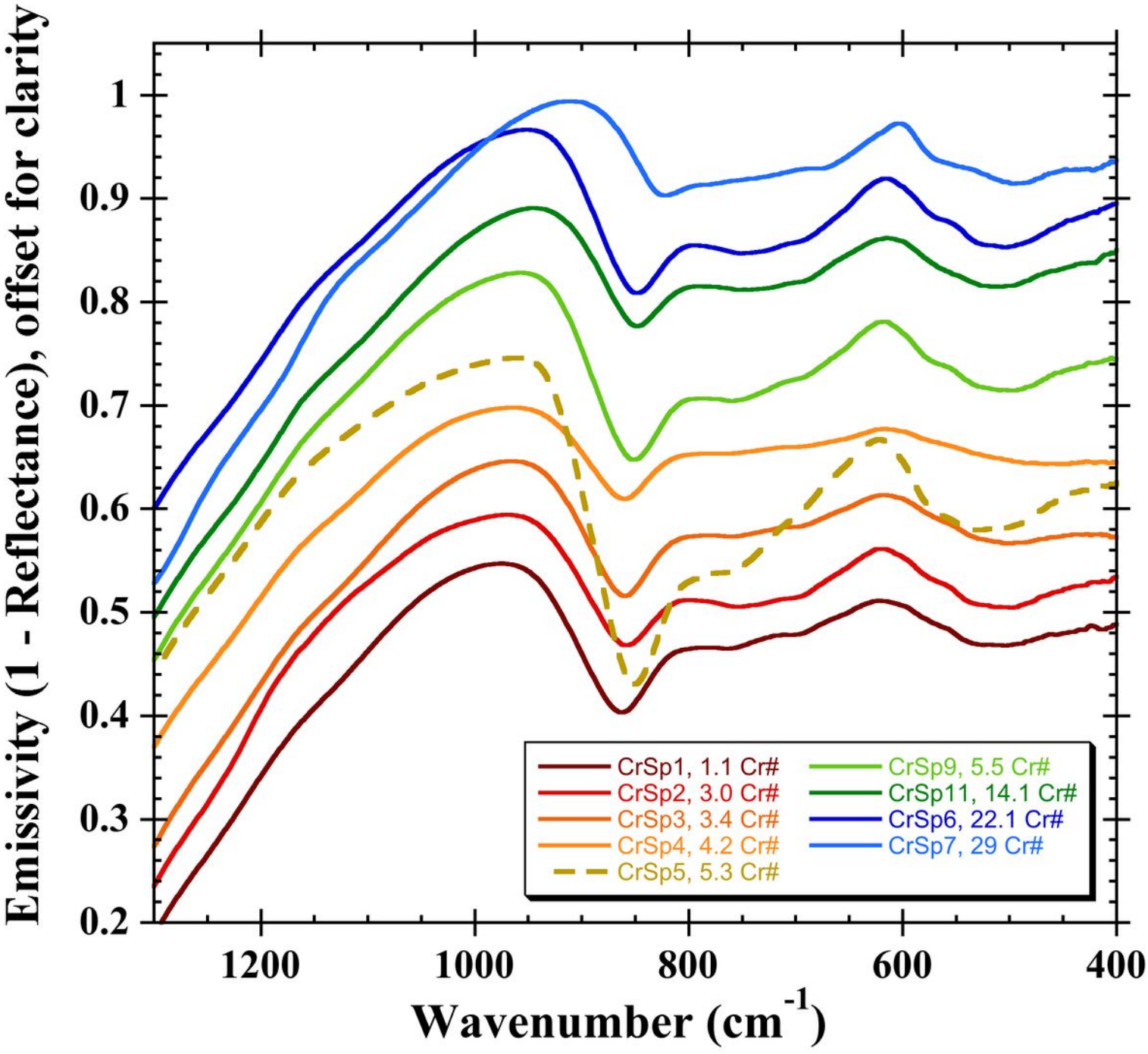
Emissivity (1 - Reflectance), offset for clarity
1
0.9
0.8
0.7
0.6
0.5
0.4
0.3
0.2
1200
1000
800
600
400
Wavenumber (cm-1)
CrSp1, 1.1 Cr#
CrSp2, 3.0 Cr#
CrSp3, 3.4 Cr#
CrSp4, 4.2 Cr#
CrSp5, 5.3 Cr#
CrSp9, 5.5 Cr#
CrSp11, 14.1 Cr#
CrSp6, 22.1 Cr#
CrSp7, 29 Cr#

Figure 8

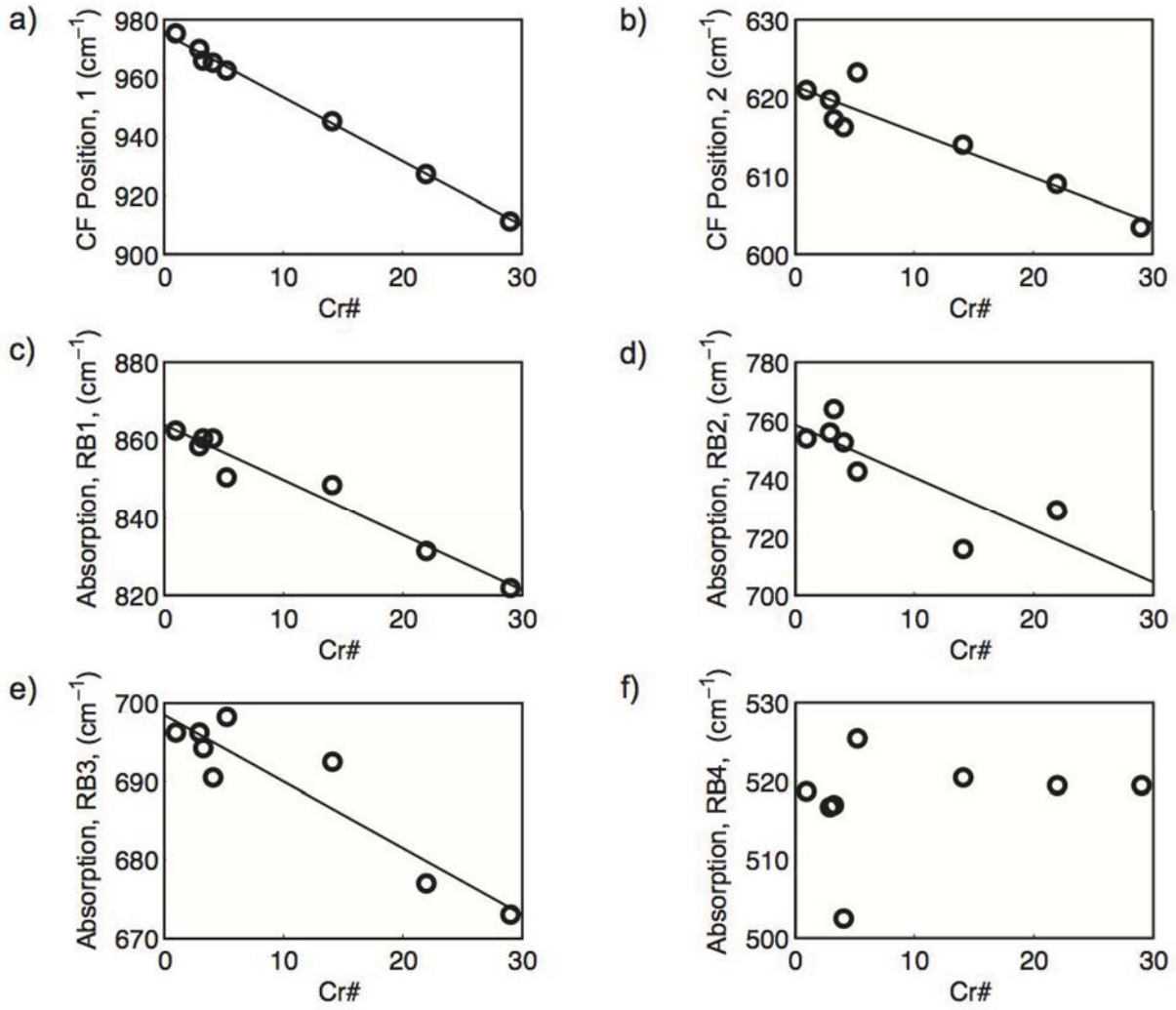
a)
CF Position, 1 (cm^{-1})
980
960
940
920
900
0
10
20
30
Cr#
b)
CF Position, 2 (cm^{-1})
630
620
610
600
0
10
20
30
Cr#
c)
Absorption, RB1, (cm^{-1})
880
860
840
820
0
10
20
30
Cr#
d)
Absorption, RB2, (cm^{-1})
780
760
740
720
700
0
10
20
30
Cr#
e)
Absorption, RB3, (cm^{-1})
700
690
680
670
0
10
20
30
Cr#
f)
Absorption, RB4, (cm^{-1})
530
520
510
500
0
10
20
30
Cr#

Figure 9

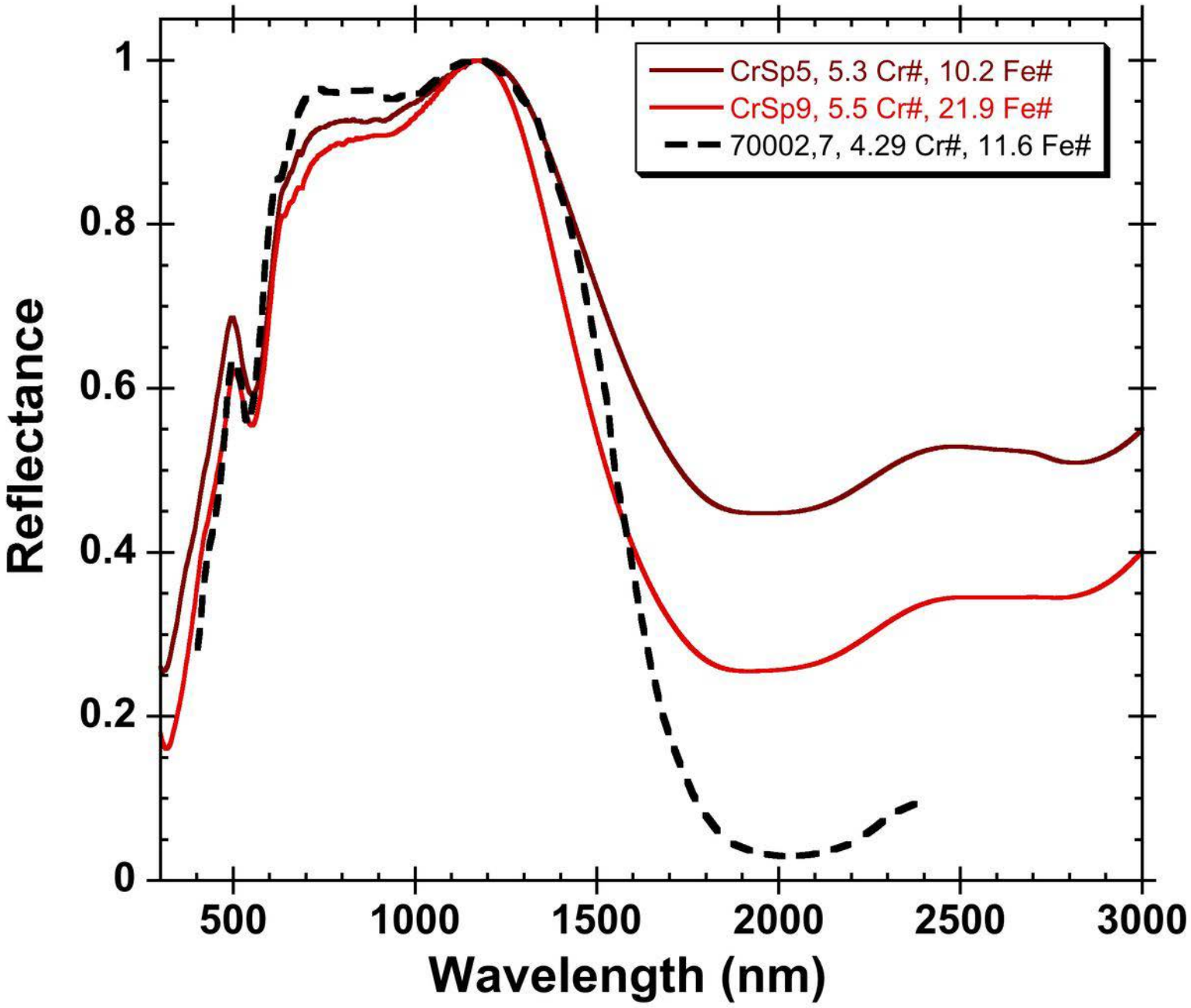
CrSp5, 5.3 Cr#, 10.2 Fe#
CrSp9, 5.5 Cr#, 21.9 Fe#
70002,7, 4.29 Cr#, 11.6 Fe#
Reflectance
Wavelength (nm)
0
0.2
0.4
0.6
0.8
1
500
1000
1500
2000
2500
3000